Wiley Online Library
Early View publication on www.wileyonlinelibrary.com
(issue and page numbers not yet assigned;
citable using Digital Object Identifier – **DOI**)

Phys. Status Solidi A, 1700020 (2017) / **DOI** 10.1002/pssa.201700020

physica status solidi a
www.pss-a.com
applications and materials science

A study of the physical properties and gas-sensing performance of TiO_2 nanofilms: Automated nebulizer spray pyrolysis method (ANSP)

Vijayan Gopala Krishnan[1,2], Annadurai Purushothaman[3], and Palaniappan Elango[*,1]

[1] Department of Physics, Government Arts College, Coimbatore 641018, India
[2] Department of Physics, Sree Sakthi Engineering College, Coimbatore 641104, India
[3] Department of ECE, Sree Sakthi Engineering College, Coimbatore 641104, India

Received 13 January 2017, revised 23 April 2017, accepted 2 May 2017
Published online 30 May 2017

Keywords automated nebulizer spray pyrolysis, FESEM study, UV study and gas sensing behavior, XRD study

[*] Corresponding author: email yuvagopal@yahoo.in, Phone: +914222215212; +918056455006, Fax: +914222217572

Automated nebulizer-sprayed TiO_2 nanofilms were deposited on the glass substrate by using different temperature (300, 350, 400, 450, and 500 °C). The effect of temperature on the structural study by XRD and AFM reveals that the amorphous nature turns to stabilized anatase tetragonal phase with an enhancement of the preferred orientation (101), particle size, average roughness of the topographical view and thickness (238, 279, 304, 362, and 397 nm) of the coated films. The morphological study by the FESEM method shows a crack and a void free micro grain particle due to the effect of temperature. An optical study shows that the transmittances of all the samples gradually decreased and the redshift of the absorption edges with decreased bandgap (3.67–3.35 eV) value is observed by the influence of temperature. The n-type semiconducting nature of TiO_2 nanofilms shows the voltage drop across the sensor element on exposure to the reducing gas. Among the various gases (CH_4O, C_3H_8O, NH_3, C_3H_6O) the reducing gas C_2H_6O exhibits a better response for a 500 °C coating temperature at an optimal operating temperature of 300 °C with a 150 ppm gas concentration.

1 Introduction Generally, an electronic nose (e-nose) is a sensor device that is used to sense the physical conditions of chemical compounds. The gas constituents were analyzed by using assorted methods but an e-nose detects the specific patterns or fingerprints of the gas mixture. The chemical sensor of the e-nose is most commonly used in conductivity sensors (metal oxide semiconductor, conducting polymer), piezoelectric sensors, MOSFET sensor, and optical sensors [1–3]. Among these, the conductivity sensor of a chemiresistor (metal oxide semiconductor) emphasizes the nature of surface sites and the surface reaction of gas, the electron-acceptor/donor properties of the gas, and adsorption and desorption of the gases. Currently, many researchers around the world are focused on studying the various metal oxide sensors (MOS). As is known, TiO_2 is considered as a prime candidate due to its numerous peculiar properties in diverse applications such as photochemical and photoconductive devices in LEDs and gas discharge displays [3], transparent conductive electrodes for solar cells [4], microelectronics [5], and gas-sensing materials for gas-sensor devices [6].

Naturally, TiO_2 occurs in three polymorphic forms: anatase (D_{4h},$^{19}I4_1$/amd-symmetry, tetragonal), rutile (D_{4h},$^{14}P4_2$/mnm-symmetry, tetragonal), and brookite (P_{cab}-lower symmetry, orthorhombic). Among the three phases, the anatase is a metastable phase and has a bandgap (3.2 eV) higher than the others. The tetragonal anatase crystal structure is made up of a chain of distorted TiO_6 octahedra, which results in a unit cell containing four Ti atoms (at positions [0, 0, 0], [0, 1/2, 1/4], and [1/2, 0, 3/4]) and eight O atoms. Moreover, the anatase phase is the most suitable candidate for gas-sensor applications due to its biological and chemical inertness, strong oxidizing power, nontoxicity and long-term stabilization against photo- and chemical corrosion, and superior charge transport [7].

Stabilization of anatase phase has been shown to be very challenging in recent research. Since the effect of the temperature and the preparation method is one of the key features that ensures phase stability, the automated nebulizer spray pyrolysis is used to ensure the prolonged anatase phase. To our knowledge, only a few studies have been carried out using acetylacetone-stabilized Ti-alkoxide precursors, whereas the phase stability was not maintained in these studies [8–10]. In particular, no systematic study of structural and optical characterization of the anatase phase TiO_2 films deposited by a spray pyrolysis technique from the catalyst of acetylacetone stabilized Ti-isopropoxide has been performed. Predominantly, the automated nebulizer sprayed anatase phase stabilized and gas-sensing performances of TiO_2 film have not been studied so far. The aim of this work is to deposit the TiO_2 nanofilms on preheated glass substrate by using different temperature (300, 350, 400, 450, and 500 °C) through automated nebulizer spray pyrolysis and exemplify the structural, optical, topography, morphological, and gas-sensing performance of the TiO_2 nanofilms.

2 Experimental

2.1 Materials deposition TiO_2 nanofilms were prepared by using an automated nebulizer spray pyrolysis technique (ANSP) with various temperatures (300, 350, 400, 450, and 500 °C) in an air atmosphere. The experimental setup, procedure and advantages of ANSP were explained [11, 12] elsewhere and Fig. 1 with optimized parameters are mentioned in Table 1. The primary stock solution was prepared with 0.1 mol l^{-1} of titanium tetra-isopropoxide (TTIP) [$Ti[OCH(CH_3)_2]_4$] dissolved in 50 ml of a mixed solution of ethanol (EtOH) (C_2H_6O) solvent with acetylacetone (AcAc) [$CH_3COCH_2COCH_3$] stabilizer in the ratio of (4:1), stirred for 15 min by using a magnetic stirrer, and finally turns into a pale yellow transparent solution. The obtained transparent pale yellow solution was poured into nebulizer container and sprayed on the ultrasonically cleaned glass substrate at various temperatures.

Table 1 Optimized spray parameter for TiO_2 nanofilms.

particulars	parameter
spray type	nebulizer
air blast	atomizer
carrier gas pressure	30 Pa
solution flow rate	0.10 ml min^{-1}
distance from substrate to spray nozzle	5 cm
substrate type	glass
solvent	ethanol and acetyle acetone
precursor	titanium isopropoxide
concentration	0.1 mol l^{-1}
deposition temperature	300, 350, 400, 450, and 500 °C

2.2 Characterization techniques The effect of temperature and their characterization were analyzed by the following means. The structural, compositional properties of TiO_2 films were entirely studied by X-ray diffraction (Bruker D8 advance X-ray diffractometer) with Cu K_α radiation ($\lambda = 0.15418$ nm) and X-ray photoelectron spectroscope (XPS). The study of surface morphology was characterized via an atomic force microscope (AFM, Model-Nanoscope E) and a field emission scanning electron microscope (FESEM, Quanta-250 FEG) applying an

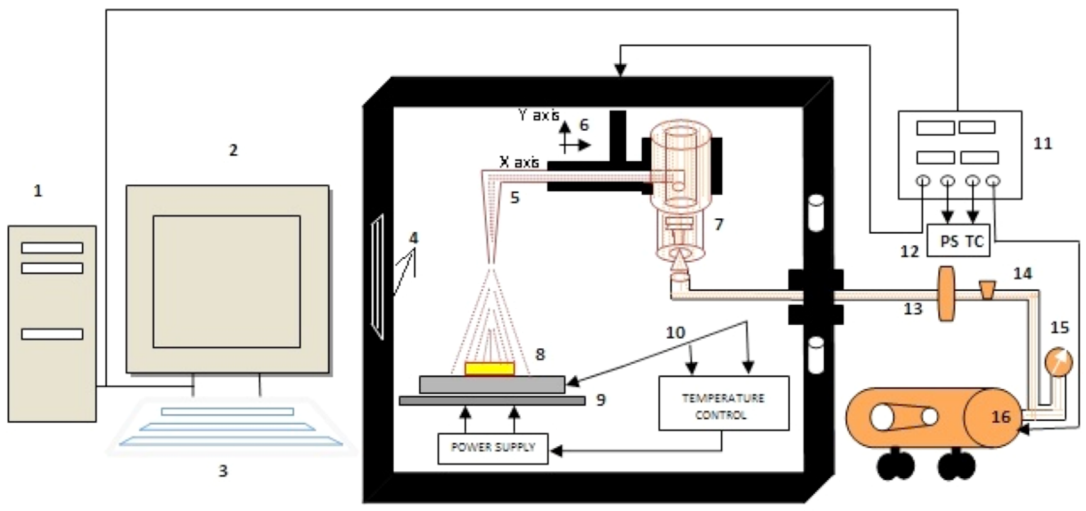

Figure 1 Schematic diagram of automated spray pyrolysis system.

operating voltage of 30.0 kV. An optical study of the films was done by an ultraviolet-visible-near-infrared (UV-Vis-NIR) spectrophotometer (Model JASCO-V-500) in the range from 250 to 970 nm, and the thicknesses of the films were determined by using surface profilometer (SJ-301 Mitutoyo). Finally, the gas-sensing performances were studied by the method of two probes with an LCR meter (GW Instek LCR – 821).

2.3 Gas-sensing measurements The schematic diagram of the gas-sensor setup is shown in Fig. 2. As can be seen, the cylindrical stainless steel testing chamber inbuilt with a nichrome-heating element and a chromel-alumel thermocouple is fixed at the bottom of the testing chamber and it is well connected with a temperature controller for adjusting the temperature (∼up to 500 °C). The sensing measurements were proceeded by a static process: a specified amount of the test gas such as C_2H_6O, NH_3, CH_4O, C_3H_8O, and C_3H_6O was injected into a testing chamber and mixed with air. A mass flow controller (MFCs) was used to control the concentration of the test gases. The sensor films were electrically connected to a two-probe setup for measurement of the resistance variation (GW Instek LCR – 821) and hence, the sensing response was calculated. The gas sensitivity response (S) factor of TiO_2 nanofilms was calculated by using the relation of resistance in the air (R_{air}) and resistance in reducing gases (R_{gas}), which was expressed as [13]:

$$S = \frac{R_{air} - R_{gas}}{R_{gas}} = \frac{\Delta R}{R_{gas}} \sim \frac{R_{air}}{R_{gas}}. \quad (1)$$

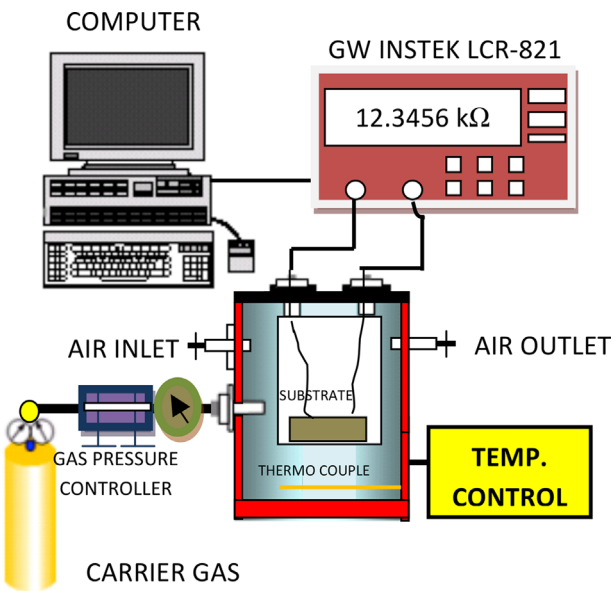

Figure 2 Schematic diagram of gas sensor setup.

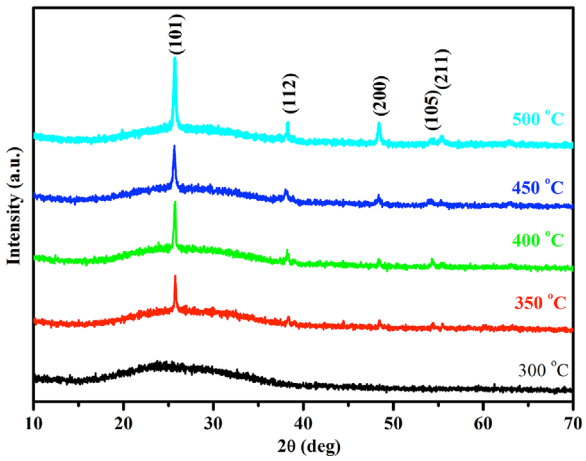

Figure 3 XRD patterns for TiO_2 thin films.

3 Results and discussion The XRD (X-ray diffraction) patterns of TiO_2 films at different temperatures are shown in Fig. 3. The obtained diffraction patterns show a predominant diffraction peak at 25.35° that can be assigned to the (101) plane of anatase TiO_2 is found to begin at approximately 350 °C. At 500 °C, a very sharp exothermic peak ($2\theta = 25.39$, 38.62, 48.19, 54.22, and 55.14°) is observed in the XRD pattern and all corresponding reflected planes (101), (112), (200), (105), and (211) were well fitted with a standard JCPDS data, card no. 89-4921. The film at 300 °C depicts an amorphous nature. This is caused by the improving crystallinity of the films. The grain size "D" is calculated using the Scherrer formula [14],

$$D = \frac{0.9 \times \lambda}{(\beta \times \cos\theta)} \quad (2)$$

$$d = \frac{n\lambda}{(2\sin\theta)}, \quad (3)$$

where D is the particle size, λ is the wavelength of the X-rays, β is the broadening of the diffraction line measured at half its maximum intensity in radians, d is the interplanar spacing value, and θ is the angle of diffraction. The obtained grain sizes of the films were increased with increasing temperature from 350 to 500 °C. This trend was confirmed by many authors [15, 16]. The lattice constants determined from the present data are $a = 3.791$ Å and $c = 9.503$ Å. The dislocation density and microstrain were calculated by using Eqs. (4) and (5) for TiO_2 films [11].

$$\delta = \frac{1}{D^2} \quad (4)$$

$$\varepsilon = \frac{\lambda}{D\sin\theta} - \frac{\beta}{\tan\theta}. \quad (5)$$

Table 2 Obtained values of structural parameters, average roughness and coating thickness of the TiO_2 films.

temp (°C)	peak position 2θ (deg)	FWHM value (deg)	(h, k, l) value			"D" particle size (nm)	"δ" dislocation $\times 10^{14}$ (linmet^{-2})	"ε" strain $\times 10^{4}$ (lin^{-2} met^{4})	"d spacing" value $\times 10^{-10}$ m	stacking fault	average roughness (nm)	thickness (nm)
			h	k	l							
300						amorphous nature					**0.062**	**238**
	25.3582	0.1673	1	0	1	50.88	3.863	7.122	3.512	0.089		
350	38.6382	0.2007	1	1	2	43.85	5.202	8.264	2.330	0.086	**1.481**	**279**
	48.1888	0.2676	2	0	0	33.99	8.654	10.659	1.888	0.101		
	25.3106	0.2004	1	0	1	42.47	5.544	8.532	3.519	0.107		
400	38.6386	0.1673	1	1	2	52.60	3.615	6.889	2.330	0.071	**1.933**	**304**
	48.1192	0.2676	2	0	0	33.98	8.658	10.662	1.891	0.101		
	25.3445	0.1337	1	0	1	63.66	2.467	5.692	3.514	0.071		
450	38.6546	0.2015	1	1	2	43.67	5.243	8.297	2.329	0.086	**2.269**	**362**
	48.1851	0.2676	2	0	0	33.99	8.654	10.659	1.889	0.101		
	25.3715	0.1171	1	0	1	72.69	1.893	4.985	3.511	0.062		
500	38.6440	0.4015	1	1	2	21.92	20.817	16.532	2.330	0.172	**2.815**	**397**
	48.1296	0.1673	2	0	0	54.36	3.384	6.665	1.891	0.063		

The calculated values are given in Table 2. It is clear that when the coating temperature is increased, the strain of the coated films increased considerably. This type of microstrain changes may be due to the predominant recrystallization process in the polycrystalline thin films.

XPS (X-ray photoemission spectroscopy) is a straightforward and nondestructive technique for the investigation of the chemical and electronic structure of materials. An important advantage of XPS is its ability to characterize the variation in the binding energies of the core level or chemical shifts of the samples. Figure 4a shows the broad emission spectrum of TiO_2 thin films in the binding energy range 0–1300 eV. Only three elements are detected on the surface of the film, titanium, oxygen and also some carbon, showing the photoelectron peaks Ti 3p, Ti 3s, Ti 2p, Ti 2s for titanium, O 1s, O 2s for oxygen, and C 1s for carbon. The high-resolution scanning images at 500 °C of TiO_2 are shown in Fig. 4b–e. In that order, separate analysis elements of core levels C 1s, O 1s, and Ti $2p_{3/2}$, Ti $2p_{1/2}$ indicated the binding energies at 286.14 eV, 530.90 eV and 458.43 eV, 465.24 eV, respectively. These calculations led to the conclusion that these titania anatase phase thin films have 7.65% of carbon, 45.16% of oxygen, 46.93% of Ti^{4+} and the presence of this prime element and carbon is probably due to the use of organic precursors and the contamination caused by sample handling [17]. The standard anatase titania (Ti^{4+}) phase was well fitted with the prepared film of TiO_2 [18].

The topographical view of a $2 \times 2\,\mu m^2$ sized three-dimensional AFM image of TiO_2 thin films using different temperatures (300, 350, 400, 450, and 500 °C) is presented in Fig. 5a–e. In the sample with the lowest temperature (300, 350, and 400 °C), the particles are rather isolated from each other (Fig. 5a–c), while those in Fig. 5d and e are widely distributed. These changes in the surface morphology might lead to a reduced crystalline quality of the films [19]. This suggests that the particles seen at the surface of the film are clusters of crystallites. The calculated values of AFM roughness parameters are listed in Table 2. This shows that the coating temperature increased with increase in the root mean square surface roughness and the coating thickness of the films, which shows the fine correspondence with XRD study of the average crystalline size and intensity. The influence of thickness significantly plays a role to control the film properties and phase stability; which is one of the important parameters to achieve the desired structural and functional properties [20]. Optical profilometer (SJ – 301 Mitutoyo) Alpha-step instruments were used to measure the coating thickness of TiO_2. The novel nebulizer spray pyrolysis method provides a uniform coating over a wide area [9] hence, the prepared films thicknesses are in the range of 238–397 nm.

The field emission scanning electron microscope (FESEM) is used to examine the morphological features such as grain morphology, thickness, grain-size distribution, and grain size of the films. The irregular granular shape of the agglomerated grain particles with dispersed large voids appeared at 300 °C (Fig. 5f) and close-packed (without pinholes) granular particles appeared at 350 °C (Fig. 5g). The cluster-like domain structure increased on increasing the coating temperature with cracks, void-free micrograin particles being revealed at 400, 450, and 500 °C.

As can be seen, the higher coating temperature can create the crystal quality and uniformity of the nanofilms,

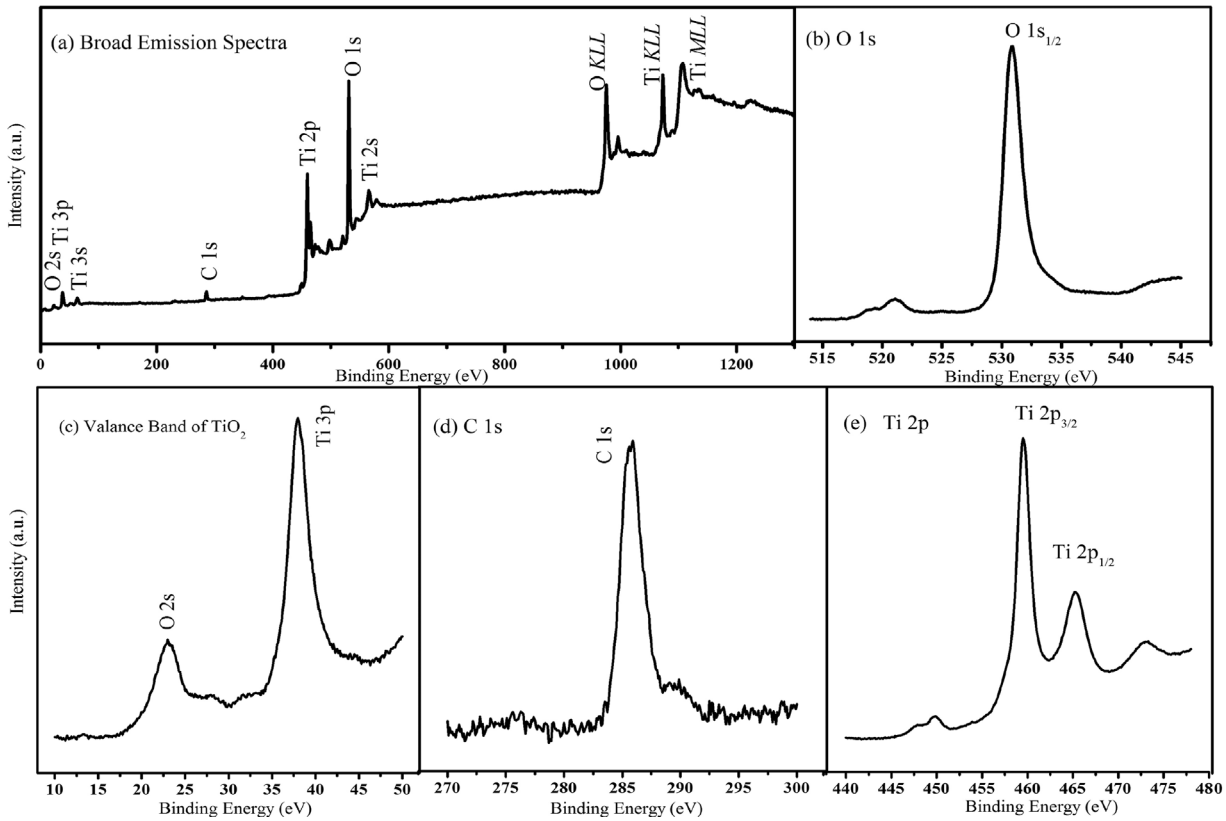

Figure 4 Survey scan XPS analysis of ($T = 500\,^{\circ}\mathrm{C}$) TiO_2 films on narrow and broad emission spectra.

which is in good agreement with the structural (XRD) and topography (AFM) study.

Optical transmittance spectra of TiO_2 films were measured in the wavelength range from 250 to 980 nm. Figure 6 shows the oscillating nature transmittance curves of TiO_2 films of different temperature (300, 350, 400, 450, and 500 °C) and the observed oscillating nature of the transmittance is due to the interference effect from the reflection at the coated films and substrates [21]. The maximum transmittance value of 102.9% (at $\lambda = 612$ nm) at 300 °C is shown in the figure, and the transmittance of all the films was decreased with increasing temperature, due to an increase in film thickness and an increase in the scattering of photons by crystal defects [22]. The calculated thickness of the coated films has been explained with the help of the following relation,

$$I = I_0 e^{-\alpha d}, \tag{6}$$

where α is the absorption coefficient and d is the films thickness. The optical absorption coefficient (α) is calculated by using [23],

$$\alpha = \frac{1}{d}\ln\left(\frac{1}{T}\right), \tag{7}$$

where T is the transmittance and d is the thickness of film. Likewise, the UV region of sharp absorption edges reveals that the redshift is due to the temperature and thickness (238, 279, 304, 362, and 397 nm). The improvement in crystal quality of the films along with a reduction in porosity [24] and their structural change is revealed by XRD measurement. For the allowed direct transition, the variation of α with photon energy ($h\upsilon$) obeys Tauc's plot [23],

$$(\alpha h\upsilon)^2 = A\left(h\upsilon - E_g\right), \tag{8}$$

where E_g is the optical bandgap, h is Planck's constant, α is the absorption coefficient, and A is a constant having values between 1×10^5 and $1 \times 10^6\,\mathrm{cm^{-1}\,eV^{-1}}$ [25]. Figure 7 shows the Tauc plot as a function of temperature in TiO_2 films. The obtained bandgap values increased from 3.22 to 3.65 eV with a decrease in the temperature. The increase in the optical bandgap with decrease in film temperature is due to the variation in lattice defects and stress [26, 27].

4 Gas-sensing behavior of TiO_2 nanofilms The sensor element of TiO_2 nanofilms exhibit typical n-type semiconducting behavior, as there is a voltage drop across the sensor element on exposure to the reducing gas. Accordingly, the gas-sensing response of TiO_2 chemiresistors (metal oxide) with different coating temperature (300, 350, 400, 450, and 500 °C) toward various gases like

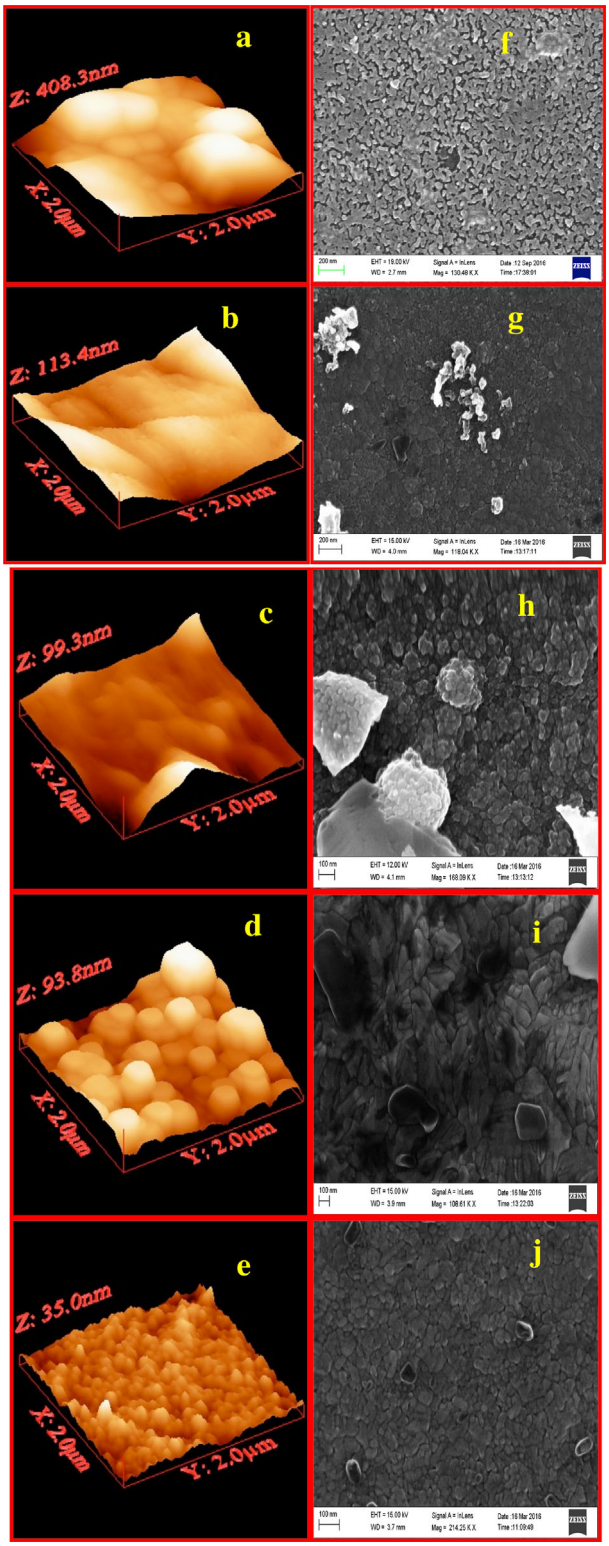

Figure 5 (a–e) Topography view of AFM and (f–j) and surface morphology of FESEM for TiO_2 thin films ($T = 300$, 350, 400, 450, and 500 °C).

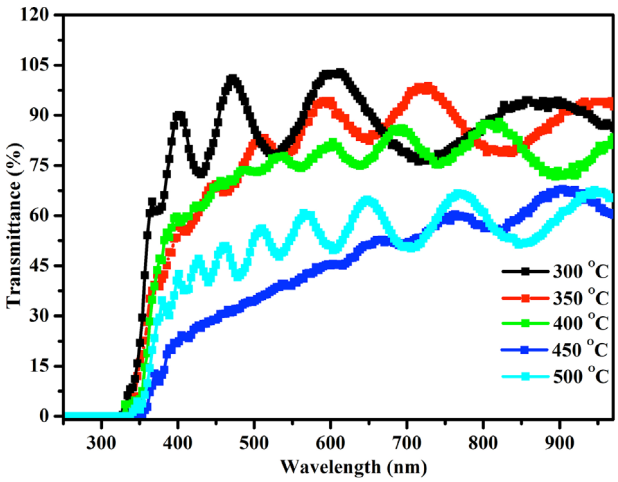

Figure 6 Optical transmittance spectra of TiO_2 films at various temperatures.

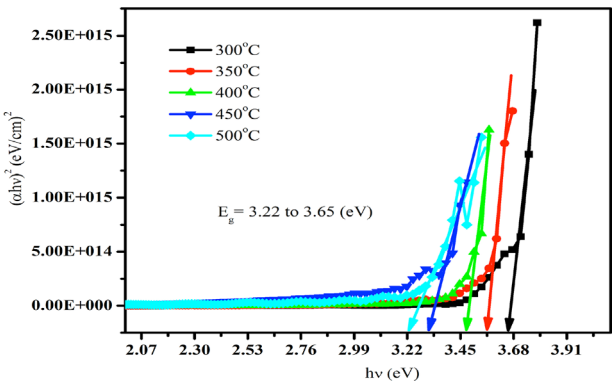

Figure 7 Plot of $(\alpha h\nu)^2$ vs. $h\nu$ for TiO_2 films sprayed using various temperatures.

methanol (CH_4O), ammonia (NH_3), isopropyl alcohol (C_3H_8O), ethanol (C_2H_6O), and acetone (C_3H_6O) reducing gas as a function of constant temperature (300 °C) and gas concentration (150 ppm) is presented in the bar chart selectivity graph of Fig. 8a. Here, the gas-sensing characteristics indicate that the sensor element exhibits the maximum sensing response to C_2H_6O reducing gas and a minimum sensing response to C_3H_8O reducing gas.

The effect of temperature on TiO_2 nanofilms when exposed to C_2H_6O reducing gas at 150 ppm constant gas concentration is presented in Fig. 8b. Hence, the various coating temperatures (300, 350, 400, 450, and 500 °C) of the sensor elements reveal the adsorption and desorption in the gas sensor by using different operating temperatures, because the sensitivity of the response increased with increasing temperature up to 300 °C, and then decreased with increasing temperature. This is due to the activation energy at a particular temperature (300 °C) being high enough to complete the chemical reaction and this temperature is called the optimal temperature. Hence, coating temperature of 500 °C exhibits the greatest possible

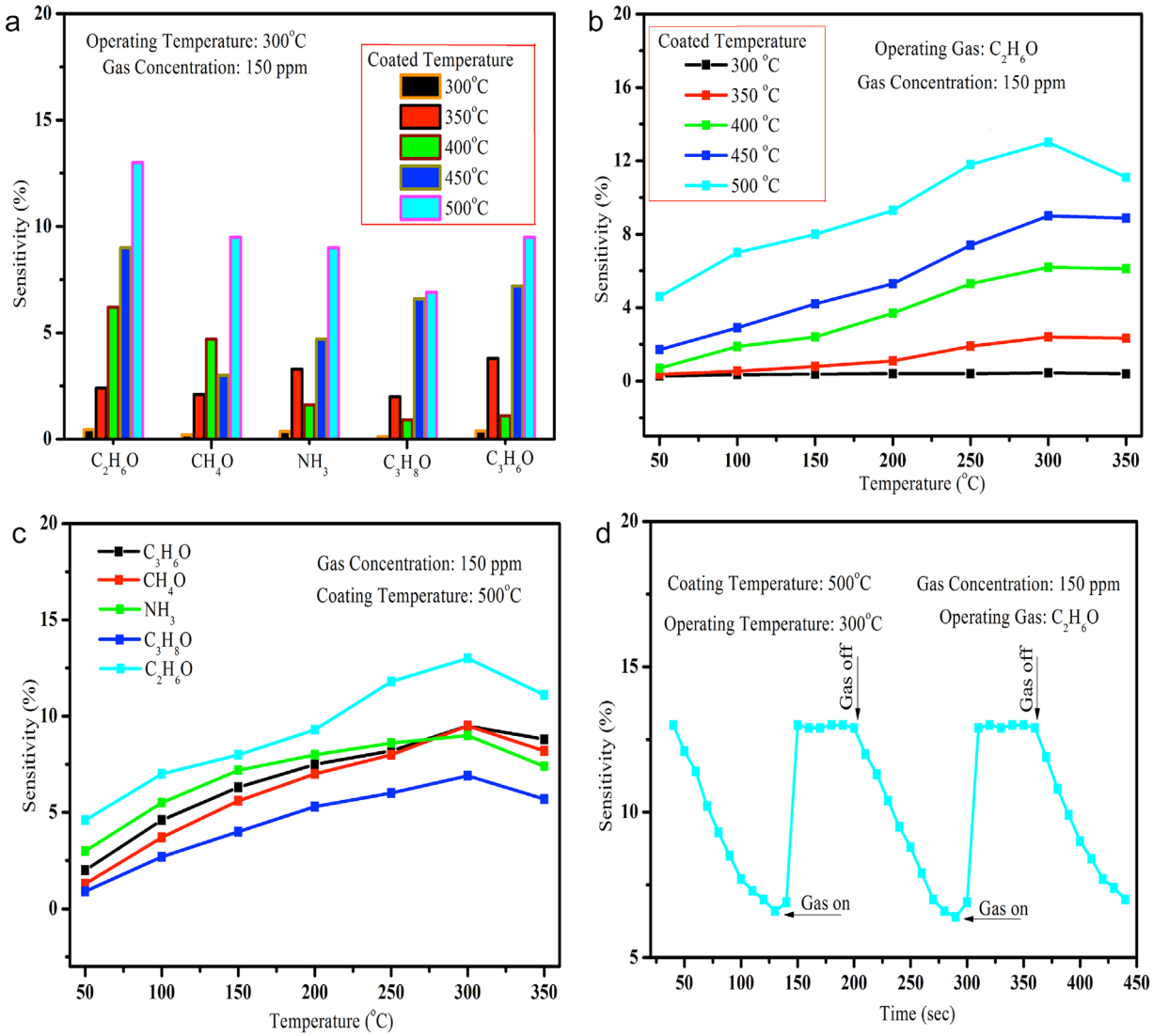

Figure 8 (a) Sensitivity of various reducing gases with constant temperature (300 °C) and concentration (150 ppm); (b) sensitivity of ethanol reducing gas at constant gas concentration (150 ppm) as a function of temperature; (c) sensitivity of various reducing gas with different operating temperature on 500 °C coated film; (d) response and recovery time of TiO_2 nanofilms.

detection to C_2H_6O reducing gas as a function of operating temperature.

The sensitivity of a chemiresistor (metal oxide) sensor is examined by the interaction of the target gas and the sensor surface. The surface-controlled process is responsible for the gas sensitivity of the metal oxide [28]. It is well known that the surfaces of metal oxides enable absorption of the oxygen species of O^-_2, O^-, or O^{2-} from the surroundings, which also control the increment of conductivity due to electron capture by the oxidizing gas at various operating temperature [29, 30] as follows,

$$O_2(\text{gas}) \rightarrow O_2(\text{ads}) \quad (9)$$

$$O_2(\text{ads}) + e^- \rightarrow O_2{}^-(\text{ads}) \quad (10)$$

$$O_2{}^-(\text{ads}) + e^- \rightarrow 2O^-(\text{ads}) \quad (11)$$

$$O^-(\text{ads}) + e^- \rightarrow O^{2-}(\text{ads}). \quad (12)$$

Oxygen may be either physisorbed as uncharged molecules (9) or chemisorbed as charged species (10–12) on the n-type semiconducting oxide surface. The physisorbed oxygen will not affect the surface states, whereas the chemisorbed oxygen species act as surface acceptors and capture the electrons from the conduction band of materials. The change of resistance is dependent on the species and chemisorbed oxygen on the surface. The surface of a TiO_2 sensor can adsorb oxygen because of the electron depletion, and the resistance of the sensor increases. The reducing

gases (R) may be adsorbed on the surface of the sensor materials according to:

$$R(gas) \rightarrow R(ads). \quad (13)$$

The reaction between the adsorbed gases and the adsorbed oxygen species, for example, O^-(ads) and O^{2-}(ads), will then proceed as follows:

$$R(ads) + O^-(ads) \rightarrow RO(ads) + e^- \quad (14)$$

$$R(ads) + O^{2-}(ads) \rightarrow RO(ads) + 2e^-. \quad (15)$$

The reducing gas (R) readily reacts with the surface chemisorbed oxygen and thereby releases electrons back to the conduction band of TiO_2, leading to a decrease in the electrical resistance of the semiconductor metal-oxide material (TiO_2). This change of the electrical resistance determines the response of TiO_2-based sensor to reducing gases. Finally, desorption of the resulting product will take place as:

$$RO(ads) \rightarrow RO(gas). \quad (16)$$

An enhanced response would be expected if a sufficient amount of target gas is adsorbed and subsequently the reaction between the adsorbed reducing gas and the oxygen species is more favorable. The gas response is directly related to the adsorbed oxygen species on the surface of the sensing layer. At higher operating temperature (>300 °C), adsorbed oxygen starts to desorb. Desorption would thus reduce the oxygen species from the surface, which in turn decreases the gas response. Thus, there exists the optimum operating temperature (300 °C) at which the gas response is higher to the sensor element of TiO_2.

Various gas-sensing responses to different gases may be due to differences in the adsorption and the reaction processes. The response of TiO_2 toward various tested reducing gases as a function of operating temperature is exhibited in Fig. 8c. From this figure, we may conclude that a sensor element based on a 500 °C coating temperature could detect well and has a poor selectivity of C_2H_6O and C_3H_8O reducing gas respectively. When a surface of the material is exposed to the reducing gas, the interaction with the chemisorbed oxygen can take place in various ways. Here, the maximum sensitivity of surface reactions can be written to C_2H_6O reducing gas as follows [31]:

$$C_2H_5OH + O_2 \rightarrow CH_3CHO + H_2O \quad (17)$$

$$CH_3CHO + O^-(ads) \rightarrow CO_2 + H_2O + e^-. \quad (18)$$

The dynamic response for ethanol reducing gas at 300 °C of optimal temperature with 150 ppm of gas concentration ($S_{max} = 12.91\%$ for 500 °C) is shown in Fig. 8d. The response (τ_{res}) and recovery (τ_{rec}) times are defined as the time it takes to decrease the maximum resistance of 90% ($R_g - R_f$) up on exposure to the target gas and then to recover the maximum resistance back to 30% when the reference gas is restored [32]. The evaluated average response (~10 s) and recovery time (~80 s) is noted, respectively. In summary, all the coated films exhibit a relatively small response to ethanol (C_2H_6O) reducing gas against others (CH_4O, C_3H_8O, NH_3, C_3H_6O) at 300 °C with 150 ppm gas concentration. The sensitivity percentage increased with increase in the coating temperature with respect to constant ethanol concentration (150 ppm), which is due to the observable fact of receptor function (surface phenomenon) [33] and their coated thickness [34].

5 Conclusions This study investigated the synthesis of titanium dioxide (TiO_2) anatase phase nanosized crystallites and high surface areas of the films by using an automated nebulizer spray pyrolysis method. The structural study by XRD shows that the amorphous nature turns to anatase phase with better plane orientation (101) and particle size. The compositional analysis of XPS confirms Ti^{4+} in the pure anatase phase and the topographical view (AFM) of roughness and coated thickness were enhanced on increasing the temperature. FESEM shows the agglomerated grains were changed to void-free micrograin particles and the optical study shows the decremented transmittance and redshift of absorption edges with reduced bandgap (3.67–3.35 eV). The optimal temperature of 300 °C at 150 ppm of ethanol reducing gas shows the better response of the 500 °C coated films among the others (300, 350, 400, and 450 °C).

Acknowledgements One of the authors (V. Gopala Krishnan) gratefully acknowledges Dr. T. Shripathi, Dr. U. P. Deshpande, and Er. Mohan Gangrade from the UGC − DAE CSR, Indore center, Khandwa Road, India for their scientific advice and for providing the necessary laboratory facilities to carry out this investigation.

References

[1] K. Madhusudan Reddy, L. Satyanarayana, S. V. Manorama, and R. D. K. Misra, Mater. Res. Bull. **39**, 1491–1498 (2004).
[2] M. Sugimoto, J. Am. Ceram. Soc. **82**, 269–280 (1999).
[3] B. Bharti, S. Kumar, H.-N. Lee, and R. Kumar, Sci. Rep. **6**, 32355 (2016).
[4] I. Vaiciulis, M. Girtan, A. Stanculescu, L. Leontie, F. Habelhames, and S. Antohe, Proc. Rom. Acad. Seri. A **13**(4), 335–342 (2012).
[5] G. P. Burns, J. Appl. Phys. **65**, 2095–2097 (1989).
[6] H. Tang, K. Prasad, R. Sanjinés, and F. Lévy, Sens. Actuators B: Chem. **26–27**, 71–75 (1995).
[7] M. Epifani, A. Helwig, J. Arbiol, R. Díaz, L. Francioso, P. Siciliano, G. Mueller, and J. R. Morante, Sens. Actuators B: Chem. **130**, 599–608 (2008).
[8] A. Oja, M. Mere, M. Krunks, R. Nisumaa, C.-H. Solterbeck, and M. Es-Souni, Thin Solid Films **515**, 674–677 (2006).
[9] F. D. Duminica, F. Maury, and S. Abisset, Thin Solid Films **515**, 7732–7739 (2007).
[10] H. Zabova and V. Cirkva, J. Chem. Technol. Biotechnol. **84**, 1624–1630 (2009).

[11] V. Gopala Krishnan, P. Elango, V. Ganesan, and P. Sathish, Optik **127**, 11102–11110 (2016).
[12] V. Gopala Krishnan, P. Elango, M. Ragavendar, P. Sathish, and G. Gowrisankar, Mater. Res. Express **4**(036401), 1–10 (2017).
[13] A. A. Haidrya, J. Puskelova, T. Plecenik, P. Durina, J. Gregus, M. Truchly, T. Roch, M. Zahoran, M. Vargova, P. Kus, A. Plecenik, and G. Plesch, Appl. Surf. Sci. **259**, 270–275 (2012).
[14] B. D. Cullity, Elements of X-Ray Diffraction (2nd edition) (Addison-Wesley Publishing Company, Inc., Reading, Massachusetts – Menlo Park, California London – Amsterdam – Don Mills, Ontario – Sydney, 1978).
[15] Ya-Qi Hou, Da-Ming Zhuang, G. Zhang, M. Zhao, and M.-S. Wu, Appl. Surf. Sci. **218**, 98–106 (2003).
[16] J. YuU, X. Zhao, and Q. Zhao, Thin Solid Films **379**, 7–14 (2000).
[17] R. Ayouchi, C. Casteleiro, R. Schwarz, J. R. Barrado, and F. Martín, Phys. Status Solidi C. **7**(No. 3–4), 933–936 (2010).
[18] S. K. Joung, T. Amemiya, M. Murabayashi, and K. Itoh, Chem. Eur. J. **12**, 5526–5534 (2006).
[19] M. A. Martynez, C. Guillen, and J. Herrero, J. Appl. Surf. Sci. **136**, 8–16 (1998).
[20] Y. S. Lim, J. S. Jeong, J. Bang, and J. Kim, Solid State Commun. **150**, 428–430 (2010).
[21] M. P. Bole and D. S. Patil, J. Phys. Chem. Solids. **70**, 466–471 (2009).
[22] H. Bensouyad, D. Adnane, and H. Dehdouh, J. Sol Gel Sci. Technol. **59**(3), 546–552 (2011).
[23] A. E. Jimenez-Gonzalez, J. A. S. Urueta, and R. Suárez-Parra, J. Cryst. Growth **192**, 430–438 (1998).
[24] N. M. Ganesan, T. S. Senthil, N. Muthukumarasamy, and R. Balasundaraprabhu, Int. J. ChemTech Res. **6**(5), 3078–3082 (2014).
[25] E. A. Davis and N. F. Mott, Philos. Mag. **22**, 903–922 (1970).
[26] Y. C. Lin, B. L. Wang, W. T. Yen, C. T. Ha, and C. Peng, Thin Solid Films **518**, 4928–4934 (2010).
[27] R. Ghosh, D. Basak, and S. Fujihara, J. Appl. Phys. **96**, 2689–2692 (2004).
[28] F. Chu, X. Q. Liu, and G. Y. Meng, Mater. Sci. Eng. B **64**, 60–63 (1999).
[29] A. A. Haidrya, J. Puskelova, T. Plecenik, P. Durina, J. Gregus, M. Truchly, T. Roch, M. Zahoran, M. Vargova, P. Kus, A. Plecenik, and G. Plesch, Appl. Surf Sci. **259**, 270–275 (2012).
[30] K. Zakrzewska, Titanium Dioxide Thin Films for Gas Sensors and Photonic Applications (AGH Ucelniane Wydawnictwa Naukowo-Dydadaktyczne, Krakow, 2003).
[31] M. R. Vaezi and S. K. Sadrnezhaad, Mater. Sci. Eng., B **140**, 73–80 (2007).
[32] Y. Li and W. Wlodarski, Sens Actuators B Chem. **83**, 160–163 (2002).
[33] S. Shukla and S. Seal, Encyclopedia of Nanoscience and Nanotechnology (Stevenson Ranc, American Scientific Publishers, CA, 2003).
[34] V. Y. Young, F. C. Chang, and K. L. Cheng, Appl. Spectrosc. **1**(l), 994–1000 (1987).